2D Monochromatic X-ray Imaging for Beam Monitoring of an X-ray Free Electron laser and a High-Power Femtosecond laser

H. Sawada[1, a)], J. Trzaska[1], C. B. Curry[2,3], M. Gauthier[2], L. B. Fletcher[2], S. Jiang[4], H. J. Lee[2], E. C. Galtier[2], E. Cunningham[2], G. Dyer[2], T. S. Daykin[1], L. Chen[1], C. Salinas[1], G. D. Glenn[2,5,6], M. Frost[2], S. H. Glenzer[2], Y. Ping[4], A. J. Kemp[4], and Y. Sentoku[7]

[1)] *Department of Physics, University of Nevada Reno, Reno, NV, 89557, USA*
[2)] *SLAC National Accelerator Laboratory, Menlo Park, CA, 94025, USA*
[3)] *Department of Electrical and Computer Engineering, University of Alberta, Edmonton, AB, T6G 1H9, Canada*
[4)] *Lawrence Livermore National Laboratory, Livermore, CA, 94550, USA*
[5)] *Department of Applied Physics, Stanford University, Stanford, California, 94305, USA*
[6)] *Center for High Energy Density Science, Department of Physics, The University of Texas at Austin, Austin, Texas, 78712, USA*
[7)] *Institute of Laser Engineering, Osaka University, Osaka, 565-0871, Japan*

a) hsawada@unr.edu

Abstract

In pump-probe experiments with an X-ray Free Electron Laser (XFEL) and a high-power optical laser, spatial overlap of the two beams must be ensured to probe a pumped area with the x-ray beam. A beam monitoring diagnostic is particularly important in short-pulse laser experiments where a tightly focused beam is required to achieve a relativistic laser intensity for generation of energetic particles. Here we report demonstration of on-shot beam pointing measurements of an XFEL and a Terawatt class femtosecond laser using 2D monochromatic Kα imaging at the Matter in Extreme Conditions end-station of the Linac Coherent Light Source. A thin solid titanium foil was irradiated by a 25-TW laser for fast electron isochoric heating, while a 7.0 keV XFEL beam was used to probe the laser-heated region. Using a spherical crystal imager (SCI), the beam overlap was examined by measuring 4.51 keV Kα x rays produced by laser-accelerated fast electrons and the x-ray beam. Measurements were made for XFEL-only at various focus lens positions, laser-only and two-beam shots. Successful beam overlapping was observed on ~58% of all two-beam shots for 10 μm thick samples. It is found that large spatial offsets of laser-induced Kα spots are attributed to imprecise target positioning rather than shot-to-shot laser pointing variations. By applying the Kα measurements to X-ray Thomson scattering measurements, we found an optimum x-ray beam spot size that maximizes scattering signals. Monochromatic x-ray imaging with SCI could be used as an on-shot beam pointing monitor for XFEL-laser or multiple short-pulse laser experiments.

I. INTRODUCTION

X-ray Free Electron Lasers (XFEL) combined with high-power optical lasers have introduced ultrafast time-resolved diagnostics capabilities to high energy density (HED) plasma experiments. Such capabilities are currently available at the Matter in Extreme Conditions end-station (MEC) [1,2] of the Linac Coherent Light Source (LCLS) [3], SPring-8 Angstrom Compact free electron LAser (SACLA) [4,5] and European XFEL [6]. At the MEC end-station, a variety of XFEL-based techniques have been used to diagnose samples irradiated by optical laser beams such as x-ray diffraction [7,8,9], x-ray absorption near edge spectroscopy [10], small-angle x-ray scattering [11], wide-angle x-ray scattering [12], x-ray phase-contrast imaging [13] and x-ray Thomson scattering (XRTS) [2].

The requirement of an x-ray beam spot size depends on the diagnostic techniques. A small x-ray spot ensures the probing of a relatively uniform sample condition. For XRTS, however, a probe beam size must be carefully chosen to strike a balance between maximizing the number of scattering photons proportional to a probe volume and avoiding scattering from too large non-uniform plasmas. Unlike long-pulse laser experiments where a laser-driven shockwave creates a large pumped region (> ~100 μm in radius), the use of a high intensity, short-pulse laser for plasma creation imposes additional complications. To achieve a relativistic intensity (> ~10^{18} W/cm^2), a beam is required to tightly focus to a spot of the order of ~10 μm for Joule class lasers. Such a small focal spot is highly sensitive to thermal drifts and mechanical vibrations, causing spatial fluctuations of the beam pointing. [14] Furthermore, inaccuracy of sample positioning leads to a low peak laser intensity as well as a spatial offset of the x-ray probe path. Measurements of short-pulse, laser-

pumped area are also important because it is larger than the laser spot due to divergence of laser-accelerated charged particles (fast electrons or energetic protons).

Spatial overlap between a FEL beam and an optical laser is commonly achieved using a cerium-doped yttrium aluminum garnet (Ce:YAG) screen or a painted-on phosphor in the sample plane. [15,16,17,18,19] Such a beam viewing screen is inserted in the interaction region and optical radiation from the screen induced by the x-ray and optical laser is recorded with a CCD camera. This measurement method is not available for full energy shots or non-phosphor targets. For time resolved XRTS measurements, x-ray scattering signals from a target of interest and monitoring of two beams in the target plane must be measured on a same target shot. Full energy beams are required to maximize scattering signals and to measure the size of a pumped region. In addition, real-time beam overlap monitoring is required on every shot in order to construct a time history of plasma conditions inferred from XRTS spectra.

In this paper, we report a novel application of 2D monochromatic imaging for simultaneous beam pointing monitoring of an XFEL and a relativistic femtosecond (fs) laser by measuring XFEL- and laser-induced Kα x rays with a spherical crystal imager (SCI) [20,21,22,23]. Irradiation of an XFEL and/or a high-power optical laser on a solid metal produces characteristic Kα x rays through photoionization and electron impact ionization, indicating the x-ray beam profile if it is in the linear photoabsorption regime and the area ionized by fast electrons. Using the measured 2D Kα photon distribution, we have quantitatively evaluated changes in x-ray probing areas at various focus lens positions, spatial fluctuations of the optical laser pointing, and a success rate of spatial overlaps of the XFEL and the fs optical laser on two-beam (XFEL+fs laser) shots. As an application of the Kα imaging diagnostic, we have also presented how Kα images and yields help to optimize an x-ray beam spot for X-ray Thomson scattering experiments in Sec. IV.

II. EXPERIMENT

The experiment was carried out using the FEL beamline and the 25 TW femtosecond optical laser available at the MEC instrument [24]. Figure 1 shows a schematic of the experimental layout with the beam and diagnostic configuration. Solid titanium samples with 2 or 10 μm thickness were laser-cut into three different sizes: 1 mm^2 square, 1.5 mm × 200 μm or 1.5 mm × 40 μm rectangular strips. [25] These samples were mounted on a translation stage set at 45° with respect to the incoming x-ray beam. The XFEL beam based on self-amplified spontaneous emission (SASE) at a photon energy of 7.0 keV was focused by a stack of nine beryllium compound refractive lenses (CRL) with 500 μm radius of curvature. Alignment of the x-ray beam to a pin at the target chamber center (TCC) was performed using a 20 μm thick Ce:YAG scintillator coupled with a combination of an optical camera (Andor Neo 5.5 sCMOS), microscope

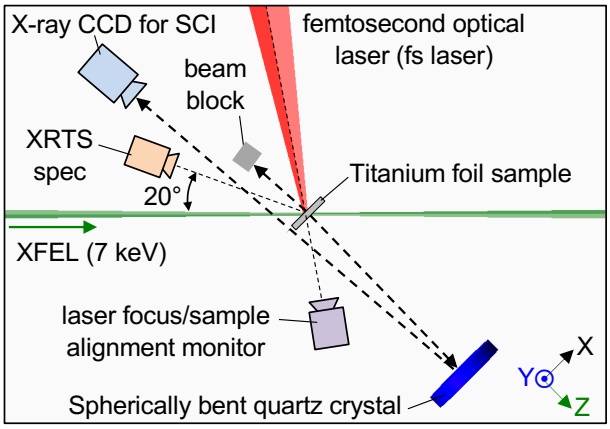

Figure 1 A schematic of the experimental layout at the MEC end station. A spherical crystal imager (SCI) consists of a spherically bent quartz crystal, an x-ray CCD and a beam block. Scattering photons were recorded with an X-ray Thomson Scattering spectrometer (XRTS spec) based on a cylindrically curved Bragg crystal. An optical camera along the laser axis was used to monitor the positioning of a titanium sample.

objective and a tube lens. The x-ray pulse energy and duration were ~4.0 mJ and ~50 fs.

The MEC's femtosecond laser at a wavelength of 800 nm delivered a beam energy up to 0.8 J in a 40 fs FWHM pulse duration. The beam was focused with a f/5 off-axis parabolic mirror to a sample positioned at TCC at an incident angle of ~40° from the sample normal. The spot size in the focal plane was imaged with an optical camera in conjunction with an apochromat 2-inch aperture objective lens providing a 0.184 μm/pixel resolution. The same imaging system was used as a sample alignment monitor. An analysis of measured beam profiles shows 30% of the beam energy contained within a 10 μm in radius. Based on the measured parameters, the peak laser intensity was estimated to be $1\sim2\times10^{18}$ W/cm^2 in this experiment. According to the ponderomotive scaling [26] based on the peak laser intensities, a mean energy of fast electrons characterized by a slope of the electron spectrum is estimated to be 65~100 keV.

The monochromatic crystal imager consisted of a spherically bent quartz crystal for 4.51 keV Titanium Kα, an x-ray CCD detector (PI-MTE:1300B) and a direct beam block. The specifications of the crystal deployed were the Miller indices of 20-23, a curvature of 250 mm and a corresponding Bragg angle of 89.0° for 4.51 keV photons. The magnification of the imager was 7.5. The camera's 20 μm pixel size together with the magnification provided a 2.6 μm per pixel resolution at TCC. Based on past experiments using the same quartz crystal [23,27,28], the nominal resolution of the crystal imager is ~15 μm, which is adequate to resolve XFEL- and laser-produced Kα emissions in this experiment as shown later. The entrance of the detector was covered by a 10 μm thick Ti and a 25 μm thick Al foil to reduce background signals. Direct

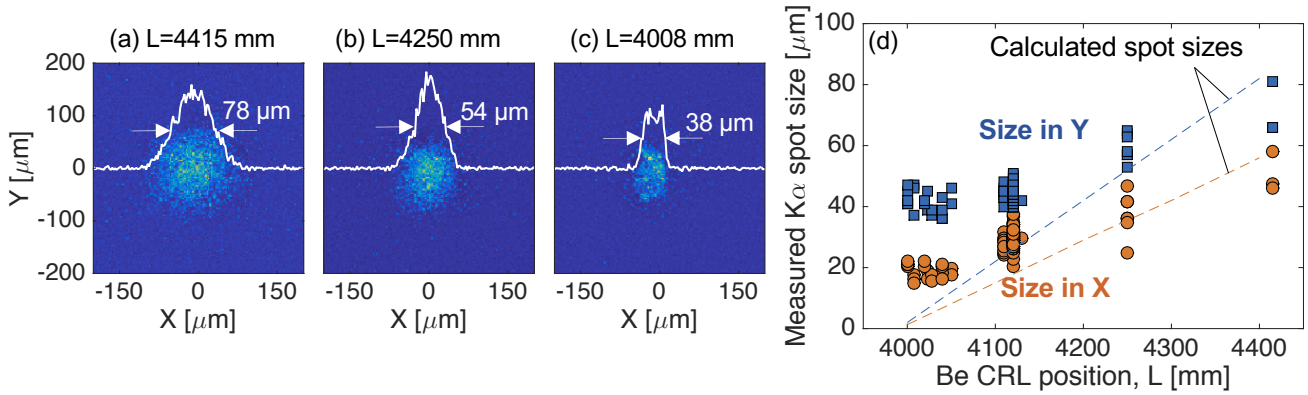

Figure 2 Kα x-ray images at the Be CRL position of (a) L=4415 mm, (b) 4250 mm, and (c) 4008 mm. (d) Measured Kα spot sizes in FWHM. Calculated spot sizes in X (orange) and Y (blue) are shown in dotted lines.

light from the laser-sample interaction to the camera was blocked by a metal beam stop.

Scattered x-ray photons were measured with a Bragg crystal spectrometer for x-ray Thomson scattering. It consisted of a cylindrically curved highly annealed pyrolytic graphite (HAPG [29]) having 32×30 mm^2 size and 51.7 mm radius of curvature coupled with an ePix100 detector [30]. The spectrometer was fielded in a backscattering geometry with a scattering angle of 160°. 7.0 keV photons undergo scattering from individual free electrons in this non-collective scattering regime [31] and form a scattering spectrum consisting of an elastic Rayleigh peak and an inelastic Compton peak. The ratio of the peaks relates to the ionization state, while the width of the Compton peak depends on the electron/Fermi temperature. The Compton downshifted energy for the scattering angle is 186 eV.

III. EXPERIMENTAL RESUTS

A. Measurements of XFEL beam profiles for various focus lens positions

Figure 2 (a-c) shows 2D Kα x-ray images produced by irradiation of the XFEL beam at various focus lens positions, L, and intensity lineouts of the images along the X direction. In Fig. 2(a), a nearly round shape of the Kα emission pattern is observed at the lens position of 4415 mm. Measured Kα spots became smaller as the focusing lens was moved towards 4000 mm for better focusing, but the emission pattern was focused better in the Y direction (meridional plane) than in X (sagittal plane), producing a rectangular shape at L=4008 mm. The smallest Kα profile observed was ~20 × ~40 μm^2 in this experiment. Fig. 2(d) shows measured Kα spot sizes and calculated x-ray beam spot sizes as a function of the CRL positions. The measured spots were corrected by taking into account the 45° diagnostic line of sight. The x-ray beam spot size focused through the CRL was calculated based on a measured unfocused x-ray beam size (550×880 μm^2) before the CRL as an input beam. The comparison of the measured and calculated spot sizes shows a reasonable agreement at 4250 mm and 4400 mm. However, the calculated beam sizes of 1.3×2.0 μm^2 and 15×22 μm^2 at 4000 mm and 4100 mm are much smaller than the measurements.

The discrepancy of the spot sizes at L <~4200 mm observed in Fig. 2(d) could be explained by production of nonthermal electrons (photoelectrons and Auger electrons) [32,33,34] and/or nonlinear photoabsorption processes [35] due to a tightly focused high intensity x-ray beam. When a K-shell electron is photoionized by a beam of high energy photons, a vacancy can be filled with an outer electron by either a radiative or non-radiative (Auger) decay process. Because of the short time scale of the XFEL pulse, non-thermal electron distribution created by 7.0 keV photons includes electrons with higher energies than the K-shell binding of titanium (4.966 keV), producing Kα emissions. Since SCI is a time-integrated diagnostic, a small spot of XFEL-induced Kα could be masked by Kα emissions produced by the secondary electrons after the x-ray beam transits the sample. This sets a limitation of the Kα imaging technique for beam monitoring that only allows for inferring an upper limit of the beam size. As shown in Fig. 2(d), the discrepancy is observed when L < 4200 mm. A corresponding x-ray beam intensity at L=4200 mm is ~10^{17} W/cm^2 and this intensity might be a threshold limiting this technique [2.1×10^{16} W/cm^2 at L=4250 mm and 1.2×10^{17} W/cm^2 at L=4100 mm]. The threshold intensity found in this experiment is consistent with the onset of nonlinear x-ray absorption processes with the x-ray fluence > a few thousands of J/cm^2 equivalent to a peak intensity of ~6×10^{16} W/cm^2 [35]. A further experiment with x-ray intensities below the threshold by lowering the x-ray beam energy could show measurements of a smaller beam profile than the current limited size of ~20 × 40 μm^2.

B. Kα x-ray emissions produced by the optical laser

Figure 3(a) shows a measured Kα image produced by fs laser-generated fast electrons and line profiles of the image

along the X and Y axes. The lineouts are obtained by averaging the image in each direction after the background is subtracted. Measured widths of the Kα spot for all optical laser-only shots range FWHM of 54±11 μm and 66±20 μm in the X and Y directions, respectively. The spread of Kα emission region depends on the energy of fast electrons propagating in a solid titanium foil. For 65~100 keV electrons estimated from the ponderomotive scaling in this experiment, an average collisional stopping range calculated with the continuous slowing down approximation (CSDA) [36] is 23~45 μm in radius, resulting in a 46~90 μm diameter. This is consistent with the measurement and verifies the estimation of the order of the peak laser intensity. Kα signal counts increased as the laser energy was changed from 0.1J to 0.8J, but the widths of the profiles were relatively insensitive to the changes. A measurement of an escaping fast electron spectrum could be used as another indirect diagnostic to infer an on-target peak laser intensity [37,38].

Shot-to-shot variations of the optical laser pointing are assessed by examining the central position of the Kα spots. The Kα intensity profiles are neither symmetric nor Gaussian. Here, the nominal beam position is defined as the central position of a half-maximum Kα intensity contour. Figure 3(b) shows a scatter plot of laser beam pointing for all laser-only shots and the Kα image with its half-maximum intensity contour of Fig. 3(a) in the background. A red dot in the figure represents the central position of the Kα image. It is noticeable that the spatial drifts of the laser pointing in X ranging from -61 to +65 μm are much larger than those in Y from -20 to -1 μm. As will be discussed in the next section, the variations of the laser-induced Kα spot positions are due to fluctuations of the laser pointing (±10 μm) in Y and a combination of the laser pointing and sample offset in the X direction.

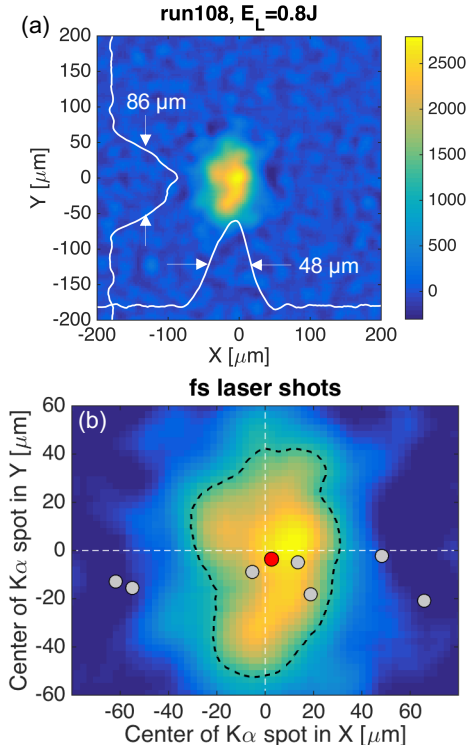

Figure 3 (a) A measured Kα image on an optical laser shot with the widths of the line profiles in X and Y (FWHM) (b) A scatter plot of measured optical beam positions inferred from the Kα emission spots. The red dot represents the central position of the background intensity shown in (a) and its half-maximum intensity contour (black dotted line).

C. Simultaneous measurements of the XFEL and optical laser beam pointing

Figure 4 shows measured Kα x-ray images and line profiles along the horizontal (X) direction on XFEL+fs laser shots for 10 μm thick samples with the surface area of 1 mm^2 for three cases: (a) overlapped, (b) laser offset and (c) sample offset. The target chamber center is indicated in the figures with a cross symbol at (x, y) = (0, 0) where both the XFEL and the fs laser were aimed. From repeated XFEL-only shots on identical samples, it is confirmed that the center of XFEL-induced Kα emissions was near the (0, 0) position within 9 μm in radius, which allows us to assume the x-ray beam passes through TCC unless a sample was offset. The image data for the two-beam shots were acquired with different timing delays between 0 and 5 ps. However, it does not affect the results of the beam pointing because the SCI diagnostic is time integrated.

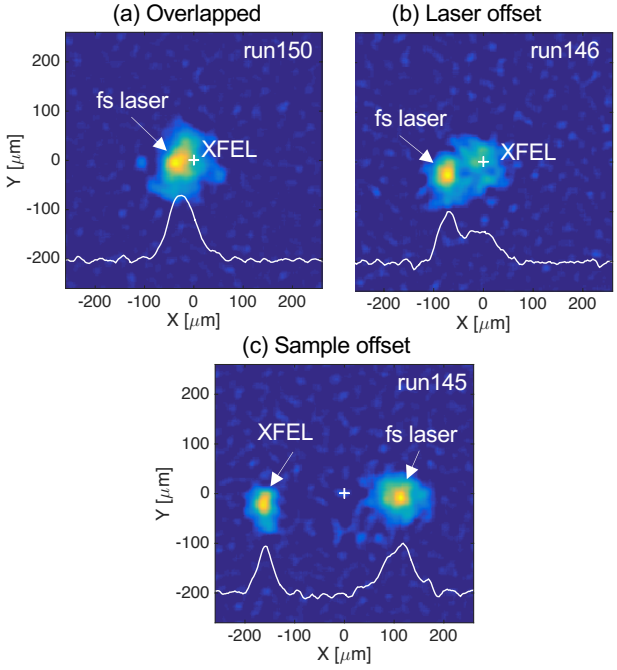

Figure 4 Measured Kα images on two beam shots. (a) The two beams were overlapped. (b) The fs laser beam was outside the x-ray beam due to the laser pointing jitter. (c) Kα spots created by both x-ray and laser beams were offset from the intended focus point due to the sample offset.

Fig. 4(a) shows an example of the two beams overlapped. In Fig. 4(b), the x-ray beam is on the cross mark, but the laser-induced Kα spot is slightly offset. The separated Kα emissions in this case are caused by a laser pointing offset because the x-ray-beam-induced Kα near the origin verifies that the sample was positioned at TCC. The beam overlaps were examined by using the Rayleigh criterion. Another case of separated Kα spots is due to an offset of the sample as shown in Fig. 4(c). A mispositioned sample along the sample monitor axis [see in Fig.1] causes drifts of the interaction points of both beams in the sample plane. Based on the measured Kα spots representing the two beams (XFEL at X=-200 μm and laser at X=~100 μm from the origin) and view angle of the alignment camera, the sample position on this particular shot is deduced to be 170 μm in the -Z direction with a rotation by 4.5° in counterclockwise direction. Well-separated Kα spots can be observed when a sample is offset in the +Z direction as well. However, the corresponding Kα would switch the positions in this case, namely the XFEL spot would appear to the right to the fs laser.

The lineout of the Kα emission intensity in Fig. 4(c) shows that the emission intensities are comparable at the 0.1 J optical laser and the 4.6 mJ XFEL beam. Lower x-ray-induced Kα intensities in Fig. 4(a) and (b) were attributed to lower x-ray beam energies of 4.0 and 3.3 mJ, respectively. Since the MEC fs laser can deliver the energy up to 0.8 J, the brightness of a laser-induced Kα spot is expected to be higher than that of an x-ray-induced. In this case, measured Kα intensities could be used to identify the laser and x-ray beam interaction positions when they are separated.

The monochromatic Kα imaging was successfully used to quantify success rates of the two-beams shots. Among the total 19 shots taken with similar laser and sample conditions, the beam overlapping was observed on 11 shots (58%). Shots for 40 μm-width strip samples were hit at a lower rate of 36%. Non-overlap shots show that the two Kα spots are separated along the X direction as shown in Fig. 4(b) and (c). This is consistent with the scatter data of the optical laser-only shots presented in Fig. 3. Because the pointing of the x-ray beam is stable, it is reasonable to conclude that the spatial drifts of the Kα spots are primarily caused by the sample positioning error rather than the pointing fluctuations of the optical laser. An accurate sample positioning system such as an additional target monitor in the orthogonal view or an automated system [39] could increase the success rate of the two-beam shots as well as shot rates on a high repetition rate laser system.

In this experiment, x-ray scattering signals on the two-beam shots were overwhelmed by strong background generated by the fs laser-target interaction even at the laser energy of 0.1J. Comparisons of x-ray scattering spectra on overlapping and non-overlapping two-beam shots as well as time-resolved x-ray scattering spectral measurements will be performed in a future experiment including an improvement of detector shielding and an optimized x-ray probe as discussed in the next section.

IV. Application of Kα imaging for X-ray Thomson scattering experiment

In addition to the beam pointing measurements, Kα crystal imaging can provide supporting information on shot-to-shot consistency and optimization of an x-ray beam spot for x-ray Thomson scattering measurements. Figure 5(a) shows integrated Kα and scattering signals for 10 μm thick titanium samples at lens positions between 4000 mm and 4250 mm along with linear least square fitting to the data. Both Kα and scattering signals linearly increase by a factor of ~3 as x-ray beam sizes are changed from 20×40 μm^2 at 4000 mm to 40×60 μm^2 at 4250 mm.

X-ray scattering spectra are affected by not only x-ray beam sizes shown in Fig. 5(a), but also sample thicknesses. Fig. 5(b) compares raw x-ray scattering spectra from cold titanium foils for 2 and 10 μm thick foils. The large and small

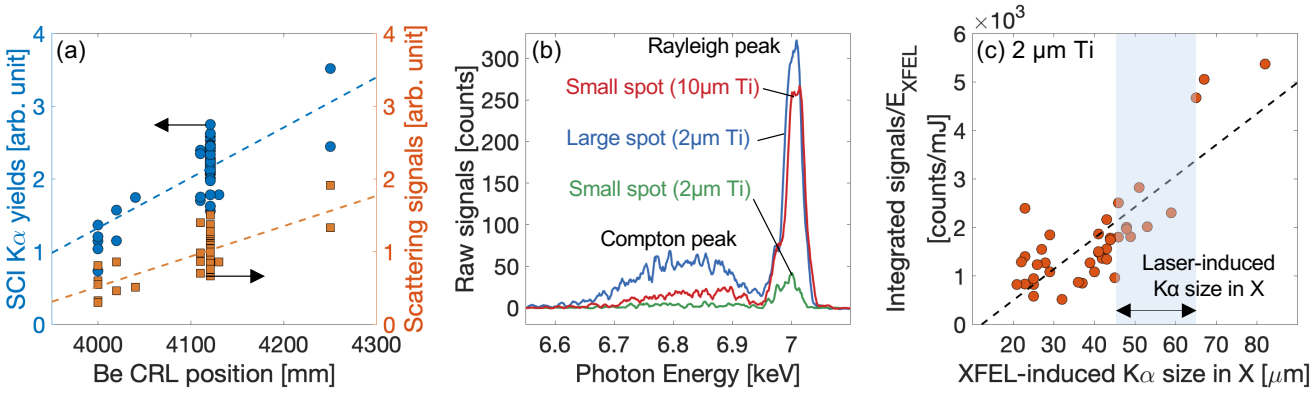

Figure 5 (a) Integrated Kα yields (blue) and x-ray scattering signals (orange) as a function of the CRL position for 10 μm thick titanium samples. (b) Measured x-ray scattering spectra from cold titanium sample. The large and small spot sizes are described in the text. (c) Normalized scattering signals divided by the x-ray pulse energy against measured XFEL-induced Kα spot size in X. The shaded area in (c) indicates the size of laser-induced Kα size. Dotted lines in (a) and (c) are calculated using linear least square fitting techniques.

x-ray beam spots indicated in the figure correspond to measured XFEL-induced Kα spot sizes of 58×81 μm^2 for Large spot (2 μm Ti), 23×42 μm^2 for Small spot (2μm Ti) and 26×45 μm^2 for Small spot (10 μm Ti). The scattering spectrum with the large spot was well above noise levels and reproduceable. The spectral shapes for the 2 μm samples agree with each other when they are normalized to the Rayleigh peak. Increasing a sample thickness from 2 μm to 10 μm with the same beam spot enhances scattering signals near 7.0 keV. However, the XRTS spectrum for the 10 μm sample does not match the other two spectra even after scaled because of wavelength-dependent attenuation by the solid sample, for instance, a 10 μm thick Ti foil transmits 23% at 6.8 keV and 26% at 7.0 keV. In addition, attenuation lengths could vary depending on where scattering occurs within a 10 μm thick sample, changing the overall spectral shape. Probing a uniform plasma condition can be ensured by using a thin sample and/or a high photon energy x-ray beam (> 10 keV) available such as at LCLS-II [40].

Fig. 5(c) shows a post-experiment analysis of a relationship between integrated x-ray scattering signals and x-ray probe spot sizes in X. The two-beam shots were taken with X=25~30 μm. Based on this analysis, an optimum x-ray spot size for the present x-ray Thomson scattering experiment is estimated to be X=43~65 μm, as the beam size would fully cover the laser-produced Kα area shown in Fig. 3. It is noted that the shape of the x-ray probe is asymmetric. The corresponding spot sizes in Y are shown in Fig. 2(d). Matching the x-ray beam spot with the pumped area would increase integrated scattering signals by a factor of 2.4~4.1 according to the fit shown in Fig. 5(c). Moreover, signal-to-noise ratios could be further improved by increasing spectrometer shielding to reduce the background and/or using a larger x-ray beam spot if the short-pulse laser spot could be enlarged while maintaining the relativistic intensity. To make this work, we will implement an improved x-ray scattering spectrometer and a hard x-ray probe at 15 keV of LCLS-II at the MEC end-station in future experiments.

V. CONCLUSIONS

Simultaneous beam pointing monitoring of the LCLS XFEL and the MEC fs laser has been successfully demonstrated using 2D monochromatic x-ray imaging with a spherical crystal imager. The XFEL- and laser-induced titanium Kα emissions were used to identify relative beam positions in the sample plane. Successful beam overlap was found to be ~58% of two-beam shots. The results reveal that the separation of the beam pointing is mainly caused by imprecise sample positioning rather than spatial fluctuation of the laser pointing. On XFEL-only shots, an agreement between the measured and calculated Kα sizes indicates that 2D emission patterns represent the x-ray beam profiles for a large spot. This imaging diagnostic, however, is limited as a beam profile monitor to measure a spot size smaller than ~20×40 μm^2, which could be attributed to nonthermal Auger electrons and/or nonlinear photoabsorption process by a tightly focused x-ray beam with an intensity above ~10^{17} W/cm^2.

The results of laser-induced Kα measurements provide information not only on the pointing of the laser beam, but also on the mean energy of fast electrons inferred from the spatial distribution. Furthermore, the experimental determination of the laser-pumped area enables users to find an optimum x-ray probe spot for X-ray Thomson scattering measurements. Target materials can be changed to others such as Cu, Ar or Zr since several spherically bent crystals matching to its Kα photon energy are available [22]. The monochromatic x-ray imaging with SCI demonstrated in this work could be used as an on-shot beam monitor in XFEL-high power laser and/or multiple short-pulse laser experiments.

ACKNOWLEDGEMNETS

Use of the Linac Coherent Light Source (LCLS), SLAC National Accelerator Laboratory, is supported by the U.S. Department of Energy (DOE), Office of Science, Office of Basic Energy Sciences under Contract No. DE AC02-76SF00515. The Matter in Extreme Conditions (MEC) instrument of LCLS has additional support from the DOE, Office of Science, Office of Fusion Energy Sciences under contract No. DE-AC02-76SF00515. This material is based upon work supported by the National Science Foundation under Grant No. 1707357 and 2010502 through the NSF/DOE Partnership in Basic Plasma Science and Engineering. Target fabrication was conducted at SLAC National Accelerator Laboratory with support from U.S. DOE Office of Science, Fusion Energy Sciences under FWP 100182. C.B.C. was partially supported by the Natural Sciences and Engineering Research Council of Canada (NSERC). The work of G.D.G. was supported in part by the U.S. Department of Energy, Office of Science, Office of Workforce Development for Teachers and Scientists (WDTS) under the Science Undergraduate Laboratory Program (SULI). Work partially performed under the auspices of the U.S. Department of Energy by the Lawrence Livermore National Laboratory under Contract DE-AC52-07NA27344 and funded by the DOE Office of Science Early Career Program under SCW 1265 and SCW 1420.

DATA AVAILABILITY

The data that support the findings of this study are available from the corresponding author upon reasonable request.

[1] B. Nagler, B. Arnold, G. Bouchard, R.F. Boyce, R.M. Boyce, A. Callen, M. Campell, R. Curiel, E. Galtier, J. Garofoli, E. Granados, J. Hastings, G. Hays, P. Heimann, R.W. Lee, D. Milathianaki, L. Plummer, A. Schropp, A.

Wallace, M. Welch, W. White, Z. Xing, J. Yin, J. Young, U. Zastrau, and H.J. Lee, J. Synchrotron Radiat. 22, 520 (2015).
[2] S.H. Glenzer, L.B. Fletcher, E. Galtier, B. Nagler, R. Alonso-Mori, B. Barbrel, S.B. Brown, D.A. Chapman, Z. Chen, C.B. Curry, F. Fiuza, E. Gamboa, M. Gauthier, D.O. Gericke, A. Gleason, S. Goede, E. Granados, P. Heimann, J. Kim, D. Kraus, M.J. MacDonald, A.J. Mackinnon, R. Mishra, A. Ravasio, C. Roedel, P. Sperling, W. Schumaker, Y.Y. Tsui, J. Vorberger, U. Zastrau, A. Fry, W.E. White, J.B. Hasting, and H.J. Lee, J. Phys. B At. Mol. Opt. Phys. 49, 092001 (2016).
[3] P. Emma, R. Akre, J. Arthur, R. Bionta, C. Bostedt, J. Bozek, A. Brachmann, P. Bucksbaum, R. Coffee, F.J. Decker, Y. Ding, D. Dowell, S. Edstrom, A. Fisher, J. Frisch, S. Gilevich, J. Hastings, G. Hays, P. Hering, Z. Huang, R. Iverson, H. Loos, M. Messerschmidt, A. Miahnahri, S. Moeller, H.D. Nuhn, G. Pile, D. Ratner, J. Rzepiela, D. Schultz, T. Smith, P. Stefan, H. Tompkins, J. Turner, J. Welch, W. White, J. Wu, G. Yocky, and J. Galayda, Nat. Photonics 4, 641 (2010).
[4] M. Yabashi, H. Tanaka, and T. Ishikawa, J. Synchrotron Radiat. **22**, 477 (2015).
[5] T. Yabuuchi, A. Kon, Y. Inubushi, T. Togahi, K. Sueda, T. Itoga, K. Nakajima, H. Habara, R. Kodama, H. Tomizawa, and M. Yabashi, J. Synchrotron Radiat. 26, 585 (2019).
[6] M. Nakatsutsumi, K. Appel, C. Baehtz, B. Chen, T.E. Cowan, S. Göde, Z. Konopkova, A. Pelka, G. Priebe, A. Schmidt, K. Sukharnikov, I. Thorpe, T. Tschentscher, and U. Zastrau, Plasma Phys. Control. Fusion 59, 014028 (2017).
[7] Z. Xing, E. Galtier, H.J. Lee, E. Granados, B. Arnold, S. Mullane, C. Bolme, A. Fry, P. Hart, and B. Nagler, X-Ray Diffraction at Matter in Extreme Conditions Endstation, (2015).
[8] D. Kraus, J. Vorberger, A. Pak, N.J. Hartley, L.B. Fletcher, S. Frydrych, E. Galtier, E.J. Gamboa, D.O. Gericke, S.H. Glenzer, E. Granados, M.J. MacDonald, A.J. MacKinnon, E.E. McBride, I. Nam, P. Neumayer, M. Roth, A.M. Saunders, A.K. Schuster, P. Sun, T. Van Driel, T. Döppner, and R.W. Falcone, Nat. Astron. 1, 606 (2017).
[9] E.E. McBride, A. Krygier, A. Ehnes, E. Galtier, M. Harmand, Z. Konôpková, H.J. Lee, H.P. Liermann, B. Nagler, A. Pelka, M. Rödel, A. Schropp, R.F. Smith, C. Spindloe, D. Swift, F. Tavella, S. Toleikis, T. Tschentscher, J.S. Wark, and A. Higginbotham, Nat. Phys. 15, 89 (2019).
[10] J. Gaudin, C. Fourment, B.I. Cho, K. Engelhorn, E. Galtier, M. Harmand, P.M. Leguay, H.J. Lee, B. Nagler, M. Nakatsutsumi, C. Ozkan, M. Störmer, S. Toleikis, T. Tschentscher, P.A. Heimann, and F. Dorchies, Sci. Rep. 4, (2014).
[11] T. Kluge, M. Rödel, J. Metzkes-Ng, A. Pelka, A.L. Garcia, I. Prencipe, M. Rehwald, M. Nakatsutsumi, E.E. Mcbride, T. Schönherr, M. Garten, N.J. Hartley, M. Zacharias, J. Grenzer, A. Erbe, Y.M. Georgiev, E. Galtier, I. Nam, H.J. Lee, S. Glenzer, M. Bussmann, C. Gutt, K. Zeil, C. Rödel, U. Hübner, U. Schramm, and T.E. Cowan, (2018).
[12] L.B. Fletcher, H.J. Lee, T. Döppner, E. Galtier, B. Nagler, P. Heimann, C. Fortmann, S. LePape, T. Ma, M. Millot, A. Pak, D. Turnbull, D.A. Chapman, D.O. Gericke, J. Vorberger, T. White, G. Gregori, M. Wei, B. Barbrel, R.W. Falcone, C.-C. Kao, H. Nuhn, J. Welch, U. Zastrau, P. Neumayer, J.B. Hastings, and S.H. Glenzer, Nat. Photonics 9, 274 (2015).
[13] S.B. Brown, A.E. Gleason, E. Galtier, A. Higginbotham, B. Arnold, A. Fry, E. Granados, A. Hashim, C.G. Schroer, A. Schropp, F. Seiboth, F. Tavella, Z. Xing, W. Mao, H.J. Lee, and B. Nagler, Sci. Adv. 5, eaau8044 (2019).
[14] G. Genoud, F. Wojda, M. Burza, A. Persson, and C.G. Wahlström, Rev. Sci. Instrum. 82, 033102 (2011).
[15] M.P. Minitti, J.S. Robinson, R.N. Coffee, S. Edstrom, S. Gilevich, J.M. Glownia, E. Granados, P. Hering, M.C. Hoffmann, A. Miahnahri, D. Milathianaki, W. Polzin, D. Ratner, F. Tavella, S. Vetter, M. Welch, W.E. White, and A.R. Fry, J. Synchrotron Radiat. 22, 526 (2015).
[16] T. Sato, J.M. Glownia, M.R. Ware, M. Chollet, S. Nelson, and D. Zhu, J. Synchrotron Radiat. 26, 647 (2019).
[17] D. Rolles, R. Boll, B. Erk, D. Rompotis, and B. Manschwetus, J. Vis. Exp. 57055 (2018).
[18] J.M. Glownia, K. Gumerlock, H.T. Lemke, T. Sato, D. Zhu, and M. Chollet, J. Synchrotron Radiat. 26, 685 (2019).
[19] H. Jang, H. Do Kim, M. Kim, S.H. Park, S. Kwon, J.Y. Lee, S.Y. Park, G. Park, S. Kim, H. Hyun, S. Hwang, C.S. Lee, C.Y. Lim, W. Gang, M. Kim, S. Heo, J. Kim, G. Jung, S. Kim, J. Park, J. Kim, H. Shin, J. Park, T.Y. Koo, H.J. Shin, H. Heo, C. Kim, C.K. Min, J.H. Han, H.S. Kang, H.S. Lee, K.S. Kim, I. Eom, and S. Rah, Rev. Sci. Instrum. 91, (2020).
[20] Y. Aglitskiy, T. Lehecka, S. Obenschain, S. Bodner, C. Pawley, K. Gerber, J. Sethian, C.M. Brown, J. Seely, U. Feldman, and G. Holland, Appl. Opt. 37, 5253 (1998).
[21] J. A Koch, O.L. Landen, T.W. Barbee, P. Celliers, L.B. Da Silva, S.G. Glendinning, B. a Hammel, D.H. Kalantar, C. Brown, J. Seely, G.R. Bennett, and W. Hsing, Appl. Opt. 37, 1784 (1998).
[22] M.S. Schollmeier and G.P. Loisel, Rev. Sci. Instrum. 87, 123511 (2016).
[23] H. Sawada, T. Daykin, H.S. McLean, H. Chen, P.K. Patel, Y. Ping, and F. Pérez, Rev. Sci. Instrum. 88, 063502 (2017).
[24] E. Cunningham, E. Galtier, G. Dyer, J. Robinson, and A. Fry, Appl. Phys. Lett. 114, 221106 (2019).
[25] M. Frost, C.B. Curry, and S.H. Glenzer, J. Instrum. 15, P05004 (2020).
[26] S. Wilks, W. Kruer, M. Tabak, and A. Langdon, Phys. Rev. Lett. 69, 1383 (1992).
[27] H. Sawada, S. Lee, T. Shiroto, H. Nagatomo, Y. Arikawa, H. Nishimura, T. Ueda, K. Shigemori, A. Sunahara, N. Ohnishi, F.N. Beg, W. Theobald, F. Pérez, P.K. Patel, and S. Fujioka, Appl. Phys. Lett. 108, 254101 (2016).
[28] H. Sawada, Y. Sentoku, T. Yabuuchi, U. Zastrau, E. Förster, F.N. Beg, H. Chen, A.J. Kemp, H.S. McLean, P.K. Patel, and Y. Ping, Phys. Rev. Lett. 122, 155002 (2019).

[29] U. Zastrau, A. Woldegeorgis, E. Förster, R. Loetzsch, H. Marschner, and I. Uschmann, J. Instrum. 8, P10006 (2013).
[30] A. Dragone, P. Caragiulo, B. Markovic, R. Herbst, B. Reese, S.C. Herrmann, P.A. Hart, J. Segal, G.A. Carini, C.J. Kenney, and G. Haller, J. Phys. Conf. Ser 493, 12012 (2014).
[31] E.E. Salpeter, Phys. Rev. 120, 1528 (1960).
[32] Y. Sentoku, I. Paraschiv, R. Royle, R.C. Mancini, and T. Johzaki, Phys. Rev. E 90, 051102 (2014).
[33] R. Royle, Y. Sentoku, R.C. Mancini, I. Paraschiv, and T. Johzaki, Phys. Rev. E 95, 063203 (2017).
[34] R. B. Royle, 2016, Kinetic modeling of ultraintense X-ray laser-matter interactions. Ph.D. diss., University of Nevada, Reno, http://unr.idm.oclc.org/login?url=https://search-proquest-com.unr.idm.oclc.org/docview/1842427531?accountid=452
[35] J. Szlachetko, J. Hoszowska, J.C. Dousse, M. Nachtegaal, W. Bachucki, Y. Kayser, J. Sà, M. Messerschmidt, S. Boutet, G.J. Williams, C. David, G. Smolentsev, J.A. Van Bokhoven, B.D. Patterson, T.J. Penfold, G. Knopp, M. Pajek, R. Abela, and C.J. Milne, Sci. Rep. 6, 1 (2016).
[36] M.J. Berger, ESTAR, PSTAR and ASTAR: computer programs for calculating stopping-power and range tables for electrons, protons and helium ions. Report NISTIR 4999 (National Institute of Standards and Technology, Gaithersburg, 1992)
[37] A. Link, R. R. Freeman, D.W. Schumacher, and L. D. Van Woerkom, Phys. Plasmas 18, 053107 (2011).
[38] H. Sawada, Y. Sentoku, A. Bass, B. Griffin, R. Pandit, F. Beg, H. Chen, H. McLean, A.J. Link, P.K. Patel, and Y. Ping, J. Phys. B At. Mol. Opt. Phys. 48, 224008 (2015).
[39] I. Prencipe, J. Fuchs, S. Pascarelli, D.W. Schumacher, R.B. Stephens, N.B. Alexander, R. Briggs, M. Büscher, M.O. Cernaianu, A. Choukourov, M. De Marco, A. Erbe, J. Fassbender, G. Fiquet, P. Fitzsimmons, C. Gheorghiu, J. Hund, L.G. Huang, M. Harmand, N.J. Hartley, A. Irman, T. Kluge, Z. Konopkova, S. Kraft, D. Kraus, V. Leca, D. Margarone, J. Metzkes, K. Nagai, W. Nazarov, P. Lutoslawski, D. Papp, M. Passoni, A. Pelka, J.P. Perin, J. Schulz, M. Smid, C. Spindloe, S. Steinke, R. Torchio, C. Vass, T. Wiste, R. Zaffino, K. Zeil, T. Tschentscher, U. Schramm, and T.E. Cowan, High Power Laser Sci. Eng. 5, e17 (2017).
[40] LCLS-II Design Study Group et al. LCLS-II conceptual design report. Technical report, Report LCLSII-1.1-DR-0001-R0, SLAC, 2014.